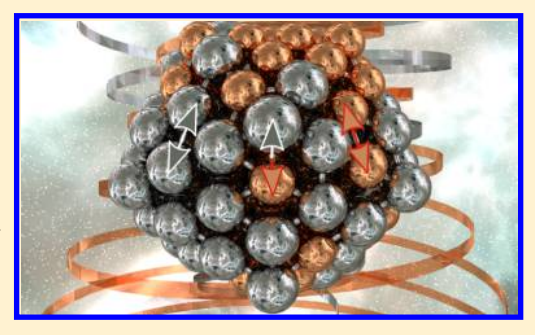
Size-, Shape-, and Composition-Dependent Model for Metal Nanoparticle Stability Prediction

Zihao Yan, Michael G. Taylor, Ashley Mascareno, and Giannis Mpourmpakis*

Department of Chemical Engineering, University of Pittsburgh, Pittsburgh, Pennsylvania 15261, United States

Supporting Information

ABSTRACT: Although tremendous applications for metal nanoparticles have been found in modern technologies, the understanding of their stability as related to morphology (size and shape) and chemical ordering (e.g., in bimetallics) remains limited. First-principles methods such as density functional theory (DFT) are capable of capturing accurate nanoalloy energetics; however, they are limited to very small nanoparticle sizes (<2 nm in diameter) due to their computational cost. Herein, we propose a bondcentric (BC) model able to capture cohesive energy trends over a range of monometallic and bimetallic nanoparticles and mixing behavior (excess energy) of nanoalloys, in great agreement with DFT calculations. We apply the BC model to screen the energetics of a recently reported 23 196-atom



FePt nanoalloys (Yang et al. Nature 2017, 542, 75-79), offering insights into both segregation and bulk-chemical ordering behavior. Because the BC model utilizes tabulated data (diatomic bond energies and bulk cohesive energies) and structural information on nanoparticles (coordination numbers), it can be applied to calculate the energetics of any nanoparticle morphology and chemical composition, thus significantly accelerating nanoalloy design.

KEYWORDS: Nanoparticles, alloys, energetics, stability

etal nanoparticles (MNPs) are a burgeoning technology, finding applications in a wide range of fields from electronics to optical devices, biological detectors and drug delivery,³ and chemical catalysis.^{4,5} MNPs are promising in large part due to their properties that differ from both the atomic and bulk size extremes, such as optical,⁶ electronic,^{7,8} magnetic,⁹ and adsoption^{10–12} behavior. These properties are dictated by the MNP morphology (i.e., size and shape) 13-16 and composition (in nanoalloys). 10,17 Beyond composition, chemical ordering at the atomic level determines important nanoalloy properties in magnetic¹ and catalytic¹⁸ applications. Deep understanding of MNP and nanoalloy stability as related to morphology, composition, and chemical ordering is therefore needed to engineer MNPs with tailored properties for specific applications.

Understanding the relationship between crystalline MNP stability and morphology began with classic Wulff theory. 19-21 Recent advances in Wulff theory extend to include bimetallic alloy mixing and surface segregation effects in crystalline bimetallic particles.²² Although powerful, Wulff construction methods (and other thermodynamic methods)²³ for MNP prediction are limited to perfect crystal shapes, whereas most MNPs contain crystal defects, 1,24 and largely cannot account for chemical ordering. Noncrystalline structures and chemical ordering in nanoalloys and MNPs can be accurately modeled using ab initio methods (i.e., density functional theory (DFT) on metal clusters). 25,26 DFT, however, becomes computationally intractable at even moderate MNP sizes (~1-3 nm diameter MNPs)²⁷ and is largely prohibitively expensive in

studying nanoalloys due to their near infinite homotops.^{28,29} For example, a single 25 atom nanoalloy structure with no identical positions (i.e., amorphous) composed of 15 Au and 10 Ag atoms has more than 3 268 760 distinct homotops. To accelerate nanoalloy analysis, several less-expensive empirical and semiempirical methods such as tight-binding models, ^{30–33} embedded atom models, ^{34,35} effective medium theory, ³⁶ and pair-wise potentials (e.g., Finnis-Sinclair³⁷ and Sutton-Chen potentials³⁸) have been developed. However, such methods require parameter tuning against large ab initio (DFT) data for accurate nanoalloy energetics, ^{39–41} limiting their broad applicability (i.e., diverse compositions) and time acceleration in analyzing nanoalloy systems. Because such empirical and semiempirical methods represent the current standard methods for rapidly screening large nanoalloy energetics, ⁴² new methods are needed to accurately and rapidly capture the energetics of diverse nanoalloy architectures and accelerate their on-demand, application-driven design.

Toward accelerated MNP energetics prediction, simple methods exist in literature relating the surface and cohesive energies (CE) of atoms in metals to their degree of coordination. 43 Coordination numbers (CN) are determined without any computational cost, relative to semiempirical or empirical methods, for any MNP structure. Surprisingly, a simple square-root bond cutting (SRB) model^{44–46} (or square-

Received: February 14, 2018 Revised: March 23, 2018 Published: March 26, 2018

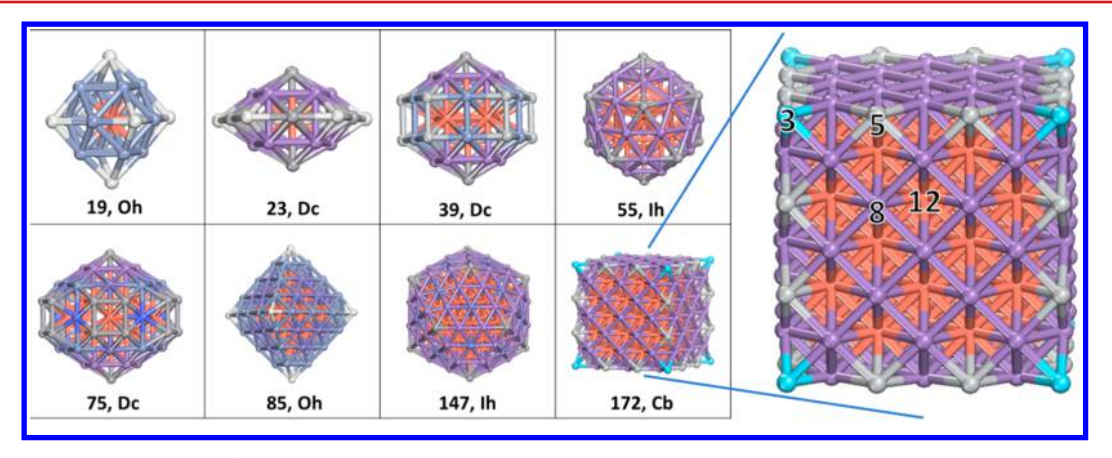


Figure 1. Metal nanoparticles (MNPs) representing different sizes and shapes (morphologies: Oh, octahedron; Dc, decahedron; Ih, icosahedron; and Cb, cubic). Atoms with different CNs are represented with different colors (color ranges from light blue for CN = 3 atoms to orange for CN = 12 atoms), as shown on the expanded 172 Cb MNP.

root CN model) can sufficiently model metal surface energetics for most transition metals compared to periodic DFT calculations, avoiding the cost of the latter. 43 Therefore, the SRB approach should also be an attractive accelerated theory for examining MNP energetics if one can accurately assign CNs for every atom on the MNP. However, until now, there were no models in literature that can accurately describe MNP energetics at practically no computational cost. Such an implementation would significantly accelerate the in silico design of MNPs (and other classes of nanomaterials)⁴⁷ and elucidate their genome. Herein, we introduce a novel, bondcentric (BC) model that accurately and rapidly determines the energetics of alloy MNPs with arbitrary morphology, composition, and chemical ordering. We first evaluated the performance of the SRB model on calculating CEs of monometallic and bimetallic MNPs using DFT calculations. It should be noticed that such a task on MNPs is missing from literature. Then, based on the performance of the SRB model, we introduce scaling factors correcting the bimetallics energetics by utilizing highly accurate bimetallic bond strength data from literature. Finally, we demonstrate the successful application of our model on effectively screening the thermodynamic stability of alloy MNPs by comparing against DFT calculations and experiments.

In applying the SRB model to MNPs, we used the CE formulated as: 44

$$CE_{MNP} = \frac{\sum_{i=1}^{n} CE_{i}}{n} = \frac{\sum_{i=1}^{n} \frac{CE_{bulk,i} * \sqrt{CN_{i}}}{\sqrt{CB_{i}}}}{n}$$
(1)

where i represents atom i in the MNP, CN_i is the coordination number of atom i, CB_i is the bulk CN of the atom i (for example, CB = 12 for face-centered cubic or fcc metals), $CE_{bulk,i}$ is the bulk cohesive energy of atom i, and n is the total number of atoms in the MNP. Note that in eq 1, the CE summation is done over all atoms and is therefore an atom-centric model and that all terms in eq 1 are readily determined for a MNP from either literature (CE_{bulk} and CB)^{48,49} or from crystal structural coordinates (CN). To increase the ease and speed of determining CN of the atoms in a MNP, we have created a Python script utilizing Atomic Simulation Environment CN0 libraries to automatically assign CN3 to atoms in any transition MNP structure. Details surrounding the automatic determination of CN3 are presented in the Supporting Information file.

To test the SRB for monometallic MNPs, we created a set of MNP structures diverse in size (19–172 atoms), shape (octahedral, Oh; decahedral, Dh; icosahedral, Ih; and cubic, Cb), and metals (Au, Ag, Cu, and Zr), as highlighted in Figure 1. We selected these MNP shapes as they represent highly symmetric and low-energy structures; 26,51 we targeted Au/Ag metals because of their ubiquity in MNP literature 2 and Cu/Zr metals due to their promise in catalysis. 52 Additionally, all of these metals have either fcc (Au/Ag/Cu) or hexagonal closepacked (hcp; Zr) bulk structures and favor close-packed (bulk CN = 12) structures, indicating that they could be theoretically stable under same MNP structures.

In Figure 2, we compare the SRB CE predictions to accurate DFT calculations on the structures shown in Figure 1. The

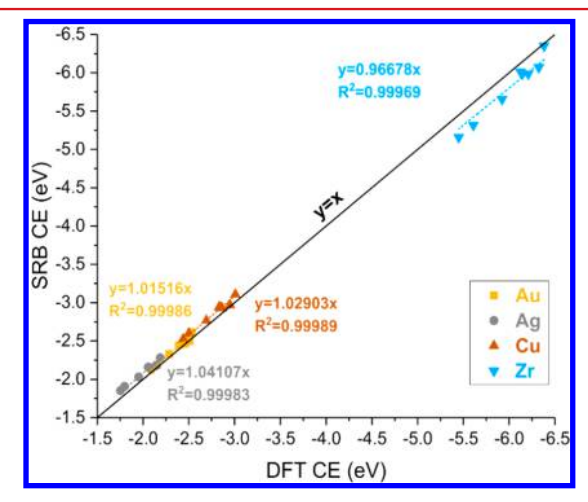


Figure 2. Parity between the cohesive energy (CE) of the SRB model vs DFT on Cu (brown triangles), Ag (gray circles), Au (gold squares), and Zr (blue triangles) MNPs shown in Figure 1.

DFT calculation details are presented in the Methods section. To directly compare DFT and the SRB method, the CE_{bulk} used in the SRB model (eq 1) is estimated from our DFT calculations using a simple $n^{-1/3}$ versus CE relation (see Figure S1a). In a comparison of the SRB to DFT utilizing a DFT-calculated value of CE_{bulk} , the SRB inherits some of the limitations of the DFT. Figure S1b shows, for example, that DFT underestimates the experimental CE_{bulk} of Ag and Au in particular. We notice in Figure 2 that the SRB model predicts

the CE of all MNPs with less than 5% error in comparison to DFT, gives high R^2 values, and trends identically to DFT for all metals. The SRB also captures the MNP CE dependence on the size and type of metal, in which larger MNPs generally show higher CEs (in absolute numbers) on the same metal and the CE follows the metal trend Zr > Cu > Au > Ag MNP (identical to DFT CE trends in Figure S1b; CE values are negative, demonstrating favorable interaction). 26 The equations of fit for the metals in Figure 2 were forced to intercept at the origin to correctly capture the limit of a single atom having a CE = 0.25 Although in Au, Ag, and Cu MNPs, we note that the CEs are slightly over-predicted, this over-prediction is likely due to nanoscale metal- and size-dependent strain that is not accounted for in the SRB model as formulated in eq 1.53 The incorporation of a nanoscale strain effect in the SRB would systematically shift the SRB energies of all MNPs slightly lower in energy (dependent on the metal and DFT functional). Contrary to the rest of the metals, we note that the CEs of Zr MNPs are under-predicted, likely because Zr is an hcp metal. In hcp metals, the (0001) plane intralayer bond lengths are not equivalent with interplane bond lengths, meaning that a bulk hcp atom more accurately has six nearest neighbors and another six near-nearest neighbors.⁵⁴ Note that the values of CB as used in the SRB model only depend on the bulk behavior of the given metal, although the Zr MNPs in this work are built from fcc-like initial structures. Thus, a CB value is likely appropriately assigned as less than 12, shifting all the SRB CE values (eq 1) higher for an hcp metal such as Zr. To preserve the simplicity and broad applicability of the SRB model, we have not included either strain or hcp stacking CB because neither metal-dependent strain⁵³ nor hcp interlayer stacking effects⁵⁴ can be readily approximated for all metals or ab initio methods. Therefore, we show that with no modifications or fitting, the SRB captures MNP energetic trends with respect to a broad range of MNP sizes.

Beyond these combined size, shape, and metal comparison tests, we assessed the power of the SRB model to capture shape differences. In Figure 3, we compare the SRB to DFT on 4

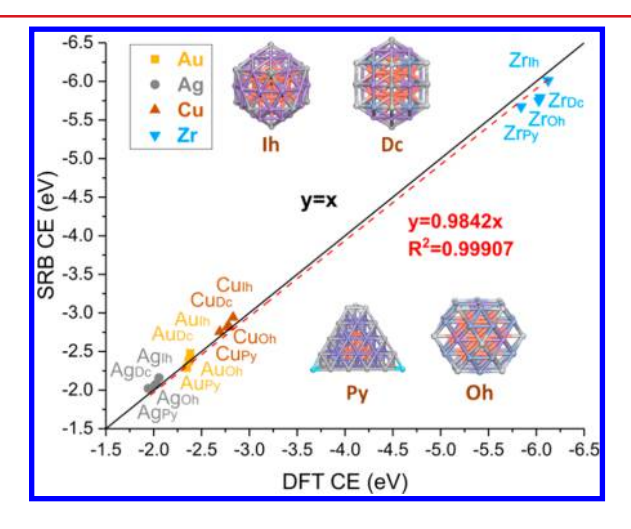


Figure 3. Parity plot between CE of the SRB model and DFT calculations of CE of MNPs of different shapes. All MNPs consist of 55 atoms, and the different shapes are illustrated as insets in the plot (Ih, icosahedron; Dc, decahedron; Py, pyramid; Oh, octahedron). Atoms with different CNs are represented with different colors (color ranges from light blue for CN = 3 atoms to orange for CN = 12 atoms), as shown in Figure 1.

MNP structures at a fixed size (55 atoms) with different shapes: icosahedron (Ih), decahedron (Dc), pyramid (Py), and truncated octahedron (Oh). We immediately observe a CE trend (Ih < Dc < Oh < Py) for all four metals that agrees perfectly with previous experimental and computational findings related to the structure of MNPs (and specifically at the 55 atom size). 26,51 Because shape differences are captured by differences in the CNs of atoms on the MNP, the smaller the MNPs the greater impact of shape on CE (Figure S2) because a higher percentage of atoms are under-coordinated at smaller MNP sizes. At 55 atoms, we are testing at a size at which shape differences can play a significant role. The SRB model thus captures shape differences between MNP structures. With the SRB effectively modeling both MNP shape and size effects, we see the SRB as an effective theory in rationalizing MNP morphology and of interest in a variety of MNP applications. 13,55

Moving past monometallic MNPs, we note that the morphology, composition, and chemical ordering of nanoalloys represent key variables for many applications 1,18 and have been the focus of heavy recent experimental study, $^{1,56-59}$ while theory has lagged experiments in its ability to rationalize nanoalloy behavior. To move beyond the atom-centric formulation of the SRB and introduce alloy effects, we introduce here a bond-centric model. This switch can be easily represented in monometallic MNPs, in which the binding energy (BE), or energy stored in the bond between atoms i and j in a MNP, can be estimated by summing the contributions of i and j to the MNP CE divided by their respective CNs (number of bonds):

$$BE_{ij} = \frac{CE_i}{CN_i} + \frac{CE_j}{CN_j} = HBE_i + HBE_j$$
(2)

where BE_{ij} represents the bond energy stored between atoms i and j, and HBE_x represents the half-bond energy contribution of atom x. The CE of an MNP is thus expressed as:

$$CE_{MNP} = \frac{\sum_{i}^{m} BE_{ij}}{n}$$
(3)

where m is the number of bonds in the MNP, and n is the total number of atoms in the MNP. We note that this formulation of the BC model (a combination of eqs 2 and 3), is mathematically identical to the SRB model (eq 1). In this simple BC formulation, we see that the SRB model assumes atoms i and j contribute equally to BE_{ij} , which appears to hold well in monometallic MNPs given the effectiveness of the SRB in capturing monometallic energetics (Figure 3). However, for nanoalloys, the assumption of equal bond energy contributions likely does not hold, as most heterolytic bonds tend to show character that favors one element over another. To incorporate an element-dependent bond weighting, we introduce two weight factors, γ_i and γ_j , to eq 2, resulting in a new expression for BE_{ij} :

$$BE_{ij} = \gamma_i \times HBE_i + \gamma_j \times HBE_j$$
(4)

where γ_i and γ_j are the weight factors for atoms i and j, respectively. Values of γ in eq 3 are calculated based on literature values of molecular dimer bond dissociation energies (BDEs). For a nanoalloy containing A and B atoms, the weighting factors of A (γ_A) and B (γ_B) for heterolytic bonds are calculated through the following system of eqs 5 and 6:

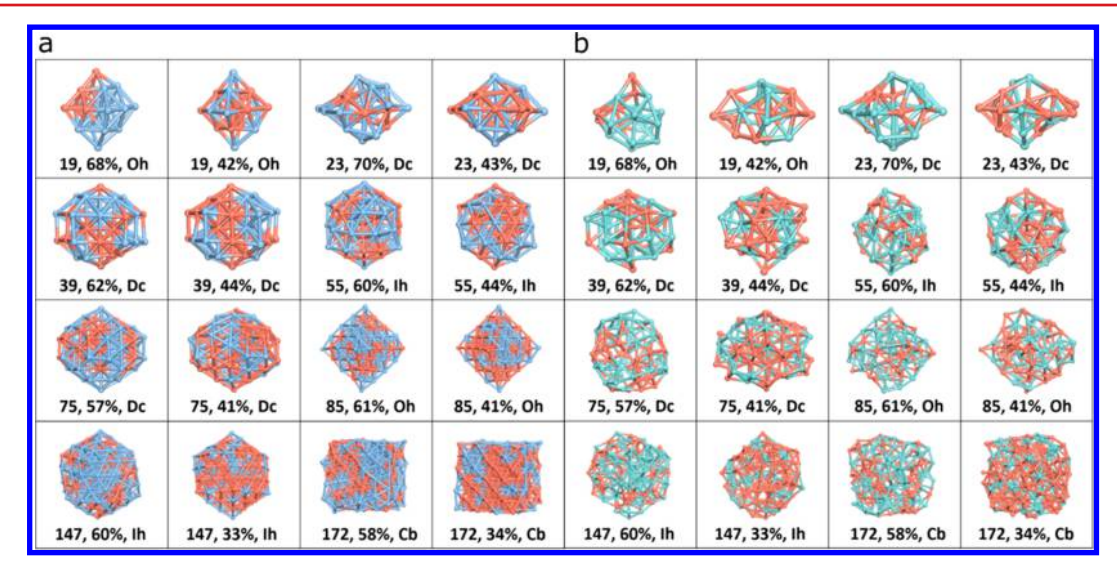


Figure 4. (a) CuAg and (b) CuZr nanoalloys of different size, shape, and composition. Structures depicted have been relaxed with DFT calculations. Red represents Cu, blue represents Ag, and green represents Zr. The label indicates MNP size (total number of atoms) and percentage of Ag/Zr in the nanoalloys (Oh, octahedron; Dc, decahedron; Ih, icosahedron; Cb, cubic).

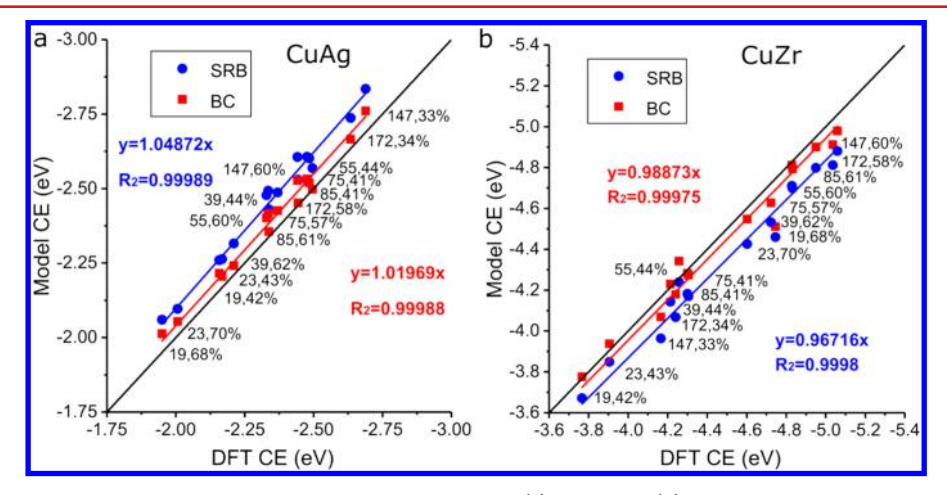


Figure 5. Parity plot between both the BC and SRB models with DFT CEs on (a) CuAg and (b) CuZr alloy MNPs. Labels indicate MNP size (total number of atoms), percent Ag in the CuAg nanoalloys, and percent Zr in the CuZr nanoalloys.

$$X \times \gamma_{A} + Y \times \gamma_{B} = 2 \times Z \tag{5}$$

where X is the experimental⁶⁰ (or theoretical)⁶¹ BDE of the A_2 bond, Y the B_2 BDE, and Z the AB BDE. Also:

$$\gamma_{\rm A} + \gamma_{\rm B} = 2 \tag{6}$$

where eq 6 is set equal to 2 for mathematical and chemical consistency with eqs 2 and 5 (as though we are breaking A_2 and B_2 to form $(AB)_2$). Experimental hetero- and homolytic dimer bond energy data are primarily used when available, whereas high-level ab initio theoretical data was used for all other cases. In a CuAg nanoalloy, for example, the BDE of a CuCu bond is 2.01 eV, a AgAg bond is 1.65 eV, and a CuAg bond is 1.76 eV, which results in (by solving eqs 5 and 6 simultaneously) $\gamma_{Ag} = 1.4$ and $\gamma_{Cu} = 0.6$ for the heterolytic bonds and $\gamma_{Ag} = \gamma_{Cu} = 1.0$ for the homolytic bonds. A total BC model is thus presented as a combination of eqs 3 and 4:

$$CE_{MNP} = \frac{\sum_{1}^{m} \gamma_{i} \times \frac{CE_{bulk,i}}{CN_{i}} \sqrt{\frac{CN_{i}}{CB_{i}}} + \gamma_{j} \times \frac{CE_{bulk,j}}{CN_{j}} \sqrt{\frac{CN_{j}}{CB_{i}}}}{n}$$
(7)

To understand the efficacy of the BC model, we test how it performs compared to the SRB model, against DFT calculations, on CuAg (Figure 4a) and CuZr (Figure 4b) alloy MNPs of different size, shape, and composition. The composition and chemical ordering of the structures in Figure 4 were randomly assigned resulting a wide test range of ordering and compositions. From Figure 4, we note the CuZr structures became more distorted (amorphous) over DFT relaxation than did the equivalent CuAg structures. To capture this restructuring accurately with CNs, we created a generalized code (made available free of charge on Github: https://github. com/mpourmpakis/bc model) that is capable of assigning CN to arbitrary bimetallic MNP structures (either amorphous or structured). Figure 5 shows the SRB and BC energetic results of both the CuAg (Figure 5a) and CuZr (Figure 5b) nanoalloys. From Figure 5, we note the BC model captures the DFT energetics more accurately than the SRB for both bimetallic systems. We calculated the average difference between the models as:

$$\operatorname{avg}_{\operatorname{diff}} = \sum_{i=1}^{N_{\operatorname{alloyMNP}}} |\operatorname{CE}_{i}^{\operatorname{BC}} - \operatorname{CE}_{i}^{\operatorname{SRB}}| \div N_{\operatorname{MNPs}}$$
(8)

The average difference between the two models is 0.07 eV/ atom in the CuAg case and 0.098 eV/atom in the CuZr case. For the smallest nanoalloy (19 atom), this represents around a 1.3-1.9 eV improvement in total alloy MNP energetics, while for the largest system (172 atom), the improvement is a substantial 12-17 eV. The difference between the models is directly related to the percentage of heterolytic bonds in the alloy MNP as the BC model is identical to the SRB for homolytic bonds, meaning that chemical ordering is factored more in the BC model than the SRB. We highlight an extreme demonstration of the effect of chemical ordering on the accuracy of the BC versus SRB models in Figure S3, in which we compare two nanoalloys with identical size (172), similar shape (cubic), and similar composition (~50% Cu/Zr). The nanoalloy that has with relatively few heterolytic bonds (Janustype) shows little difference (~0.02 eV) between the SRB and BC models, while the nanoallov with many heterolytic bonds (interlayer-mixed MNP) shows a substantially larger difference (~0.1 eV). Weighting heterolytic bonds in the BC model therefore increases its ability (relative to SRB) to accurately describe chemical ordering effects.

Our introduced BC model is a promising model for CE prediction in a wide range of nanoalloys, but we also acknowledge that it has a few inherent limitations and assumptions. One assumption in the BC is that dimer BDE trends match the CE_{Bulk} trends for metals. This means that when the dimer BDEs of elements in a heterolytic bond trend opposite their CE_{Bulk} values, the bond weighting factors (γ s) in the BC model will give incorrect CE trends for homolytic versus heterolytic bond energies. To identify cases in which this is true, we plot homolytic dimer BEs versus bulk CEs for all of the transition metals (Figure S4). Pairs of metals in Figure S4 resulting to a line with a positive slope are good candidates for the BC model, while pairs of elements with a negative slope are not. After applying this criterion to pairs of metals found in Figure S4, we found just 55 bimetallic alloys with a negative slope versus a remarkable 298 that are well-suited for the BC model. This means that around 85% of transition metal alloys can be hypothetically captured by the BC model. For example, this analysis reveals that a nanoalloy containing only Cu and Pd would not be accurately captured by the BC model, while nanoalloys that exclusively contain a subset of the elements Au, Ag, Cu, and Zr should all be accurately captured.

Beyond the broad applicability of the BC model on nanoalloys, its strong physical basis allows for important comparisons and extraction of physical learnings. For example, in Figures S5b and S6, the BC model (although it captures the CE trends between different MNPs) appears to deviate from the DFT CE for CuAu alloys. In this case, in terms of experimental BDE, we have AuCu > AuAu > CuCu and the calculated weighting factors (eqs 5 and 6) are $\gamma_{Au} = 2.36$ and γ_{Cu} = -0.36. However, the CE_{bulk} trend between Au and Cu according to DFT is opposite to the experimental CE_{bulk} trend, largely due to the DFT underestimation of the Au bulk CE (Figure S1b). Thus, the BC model appears to behave weaker than the simple SRB in comparison to DFT, although we would like to highlight that this deviation reflects error in the DFT functional performance rather than the BC model. For this reason, to further validate the BC model against experimental

behavior for the AuCu MNPs, we tested the surface segregation behavior in CuAu MNPs (Figure S7a). In the Cu₅₄Au MNP (Figure S7b), the Au is shown to have a favorable surface segregation in experiments⁶² by both the DFT and the BC model (using experimental values of CE_{bulk}) and unfavorable surface segregation by the SRB model (using experimental values of CE_{bulk}). Because the SRB model only accounts for coordination number and not chemical environment, it favors Au in the bulk state because the experimental CE_{bulk} of Au is larger than the CE_{bulk} of Cu (Figure S1). With DFT, we note that there are multiple factors contributing to a favorable Au surface segregation, given that the DFT-calculated CE_{Bulk} for Au is incorrectly less than for Cu (Figure S1), indicating that in an alloy, Au would naturally surface segregate (according to the SRB model). Therefore, the BC model alone accurately captures experimental segregation in AuCu alloy MNPs, clearly for physical reasons. Beyond AuCu, another case in which the underestimation of the CE_{bulk} of Au by DFT shifts the BC model away from parity with DFT is for AuAg nanoalloys (see Figures S5a and S8). In the AuAg nanoalloy, we highlight that both the BC and SRB models do remarkably well in capturing DFT energetics, although the SRB appears to be a slightly better match with DFT than the BC (Figure S8). Under the same assumption of the CE_{bulk} values trending with the dimer BEs used in the BC model, an underestimated CE_{bulk} for Au relative to Ag would result in a slight overestimation of the CEs of AuAg alloys MNPs (as in Figure S8). While we believe that our selection of DFT functional for this work is appropriate, the use of other, potentially more accurate functionals (depending on the metals of interest) could increase the accuracy of the SRB and BC models for capturing nanoparticle energetics versus DFT. Additionally, such an adaptation of the SRB and BC models would require only the CE_{Bulk} values for the metals of interest calculated at the new level of theory. Ultimately, we highlight that these limitations of DFT do not influence the BC model predictions when the latter is applied using only experimental CE_{Bulk} values. In addition, energy stability trends between different MNPs are most often more important than exact precision in energetic stability, and the BC model accurately captures trends in alloy MNPs.

To further test the validity of the introduced BC model, we applied it to describe the mixing energetics of metals via excess energy (EE) analysis. EE describes the preference of forming nanoalloys from structurally identical monometallic MNPs. It can be challenging to capture, 63 often requiring DFT calculations. Using the SRB and BC models, the EE 4,64 of an $A_{\rm x}B_{\nu}$ nanoalloy is calculated as:

$$EE = CE_{\text{alloyMNP}} - \frac{x}{x+y}CE_{A_{x+y}} - \frac{y}{x+y}CE_{B_{x+y}}$$
(9)

where $CE_{alloyMNP}$ is the cohesive energy of the nanoalloy, and $CE_{A_{x+y}}$ and $CE_{B_{x+y}}$ are the cohesive energies of pure A and B MNPs with x and y atoms. The derivation of this general form of eq 9 can be found in the Supporting Information. In Figure 6, we see that our BC model can capture the EE compared to accurate DFT of the nanoalloys reported in Figures 4 and 5 with an R^2 value close to 0.7 (typical threshold for statistical significance). The two points far above the parity line in the second quadrant of Figure 6 are both $Cu_{147-x}Zr_x$ nanoalloys, and these points are predicted higher in EE by the BC model, largely due to the relative overestimation of the Zr_{147} MNP CE by the SRB model (most-upper-right point on Figure 2).

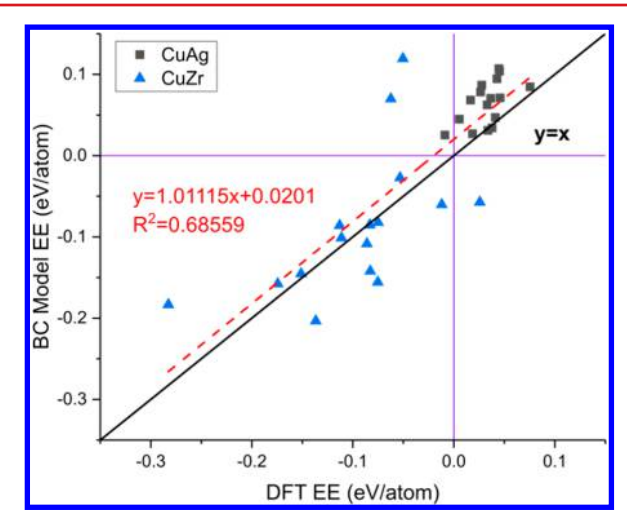


Figure 6. Parity between excess energy (EE) calculated by the BC model vs DFT of CuAg (black squares) and CuZr (blue triangles) alloy MNPs (shown in Figure 4).

Therefore, the deviation observed in Cu_xZr_y excess energies is likely more related to individual MNP structure than to model parameters. If these two points are removed, the R^2 of the equation of fit becomes greater than 0.8 (see Figure S9), highlighting the remarkable accuracy of the BC model for capturing mixing in even amorphous structures. Therefore, the BC simply, rapidly, and (relatively) accurately captures nanoalloy EE.

Utilizing the speed and ease of applying the BC model to capture EE, we tested our model on an experimental FePt nanoalloy structure containing 6569 Fe atoms and 16 627 Pt atoms recently published by Yang el.al. This nanoalloy is computationally inaccessible by current DFT methods with 23 196 atoms in total, many regional variations in chemical ordering, and many localized crystal defects and strains. Using the BC model, though, we can rapidly screen and analyze the energetics of several thousands of FePt nanoalloy architectures at this MNP size. We note that the BC model can accurately capture the FePt nanoalloy energetics as the Fe/Pt BDEs trend correctly with their CE_{bulk} values (see Figure S4). After running the CN calculation code on the experimental nanoalloy structure to create a binding topology for the nanoalloy, we developed a Python script (freely available for download on Github) to randomly distribute atoms inside the nanoalloy and calculate the resulting MNP CE and EE. Figure 7a shows the EEs of both the experimental and the generated FePt nanoalloys versus the percent of Fe using our BC model. We plot three sets of generated nanoalloys. The black squares represent the lowest-energy structures of all tested alloy MNPs for a given percent Fe, which happen to all have the Fe atoms distributed to the lowest coordination sites. The red dots show the minimum energy structure of the fully randomized structures and the blue triangles the energy of the structures with the experimental percentage of the total Fe atoms (2685/ $6569 \approx 40.8\%$) distributed on the nanoalloy surface and randomized bulk atomic positions. Except for the experimental nanoalloy, every point presented in Figure 7a represents the minimum energy of 1000 structures generated using the same criteria. In all generated nanoalloys cases, the EE is roughly parabolic with the Fe concentration, giving minima around 50% for the fully random case and around 55% for the other two cases. A minimum EE at around 50% Fe exactly matches a

recent DFT study of EE in smaller 55 atom FePt nanoalloys.⁶³ Additionally, because the EE is negative over the full compositional range, it is favorable to form intermixed nanoalloys instead of having separate monometallic NPs, which matches perfectly the experimental observations. If we look at vertical slices of the Figure 7a plot (i.e., a fixed percentage of Fe), the EE becomes more negative as the percent of Fe distributed on the surface increases (black points), indicating that Fe is generally favored toward surface segregation. The surface segregation and chemical ordering effects are further highlighted in Figure 7b, which shows a systematic analysis of surface segregation and CE. The variation within bands in Figure 7b can be considered the impact of chemical ordering at each defined MNP surface percent Fe, while the difference between bands represents the energetic impact of Fe surface segregation. Following this logic, we note that, especially at higher surface percentages of Fe, surface segregation and chemical ordering play roughly equivalent roles in determining the energetics of this alloy MNP architecture. Beyond this argument, we note that the experimental structure (green triangle in Figure 7b), which is 28.3% Fe with only 43.4% of the Fe in the surface, is very close to the minimumenergy Fe surface-segregated structure (100% of the Fe in the surface) with the same MNP composition. The experimental nanoalloy is likely preferentially formed over the surface segregated nanoalloy due to kinetic factors during growth and indicates how chemical ordering is also an important energetic factor in this FePt nanoalloy. To further explore the effect of chemical ordering in the experimental FePt nanoalloy, in Figure S10, we show the CE of a thousand generated homotops with an identical surface conformation to the experimental structure and all remaining Fe atoms randomly distributed in the bulk of the nanoalloy. We can see the distinctiveness of the experimental conformation in Figure 7b because it is several standard deviations from the norm for these randomized nanoalloys, indicating that bulk chemical ordering plays a significant role in the formation of the experimental FePt nanoalloy. To close the chemical ordering and energetic space between the experimental homotop and the random homotops (as in Figures 7b and S10), in future work, optimization techniques such as genetic algorithms with the BC model could be employed to shed more light on bulk chemical ordering trends in alloy MNPs at a fixed surface concentration. 42 Such a combination will be very powerful for the computational identification of energetically minimum MNP structures at any MNP morphology and metal composition, aiding in elucidating the MNP genome.

In summary, we have introduced a BC model able to accurately capture the energetics of MNPs as well as their mixing behavior. The BC model is orders of magnitude faster than DFT in evaluating arbitrary alloy MNPs of practically any morphology (size and shape) and metal composition. Importantly, the BC model can identify energetically preferred chemical ordering on alloy MNPs. Additionally, because the BC model does not require training to calculated or experimental parameters, it is uniquely suited to address the energetics in massive nanoalloy structures. While other thermodynamic factors such as entropy and synthesis temperature can influence nanoalloy composition and chemical ordering, we have primarily focused in this work on the enthalpic contributions (largely captured by DFT electronic energies). In our future work, we plan to include configurational entropy and temperature effects in the BC framework. Our work therefore

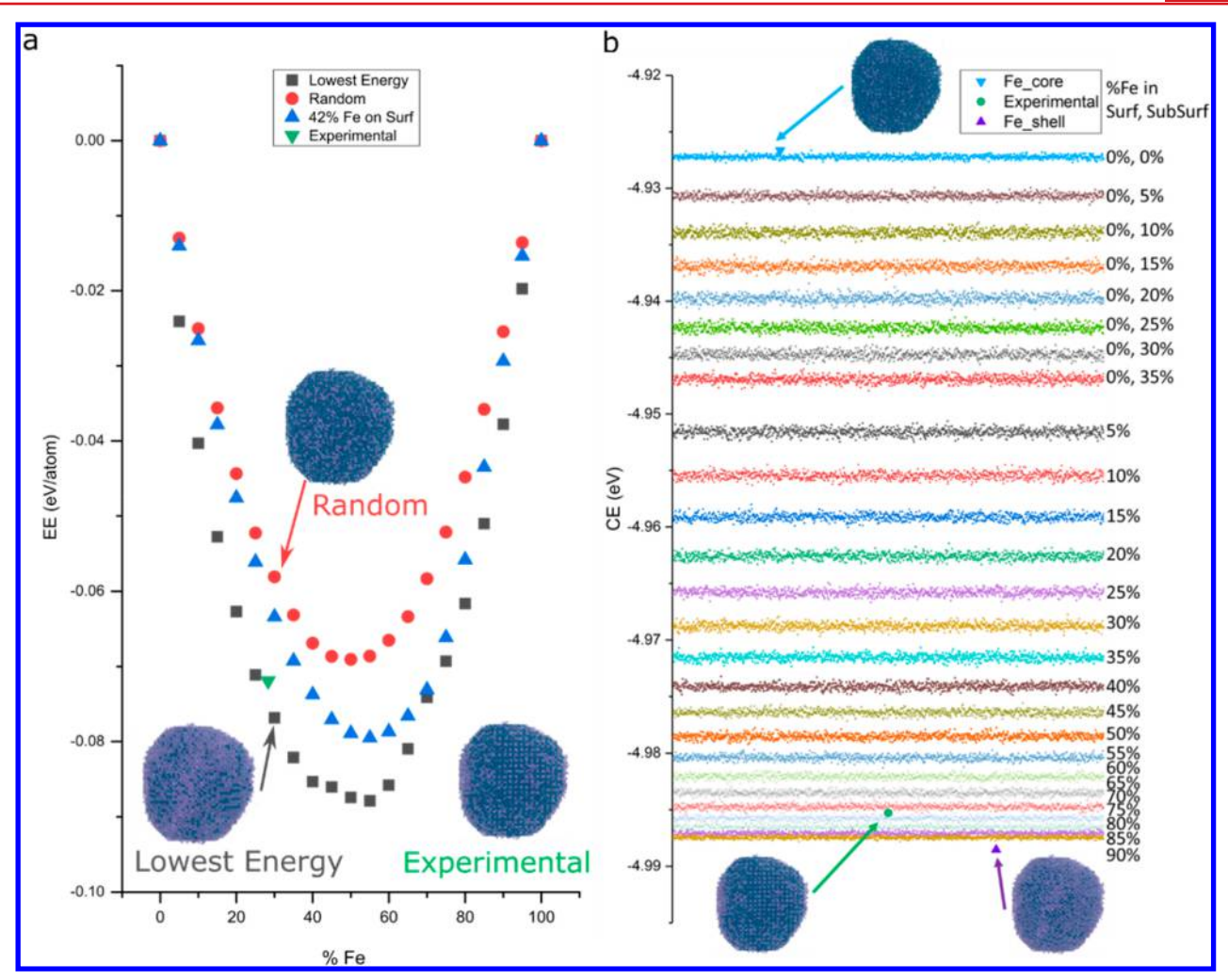


Figure 7. (a) Excess energy (eV/atom) vs percent Fe composition in the FePt alloy MNP. The black points represent the lowest-energy structures tested at each composition, which were all structures with Fe atoms placed in the lowest coordinated sites. The red points represent the minimum energy structure of 1,000 fully random homotop structures. The blue points represent the minimum energy structure of 1,000 randomly generated structures with same percent surface Fe as the experimental structure (randomly distributed in the surface) with the rest of Fe atoms equally and randomly distributed into the subsurface and bulk of the MNPs. The images shown as insets are examples at the experimental composition of the random, lowest-energy, and experimental structures in which Fe is shown in dark blue and Pt is shown in purple. (b) CEs of randomly created homotops of the experimental FePt nanoalloy. The purple triangle represents a Fe-shell structure (i.e., black point in panel a), while the light blue triangle represents a Fe core structure in which all Fe atoms are in the bulk of the MNP. Each band represents 1000 randomly created structures with specific percentages of surface, subsurface, and bulk atoms occupied by Fe atoms. All structures contain same Pt-to-Fe ratio. The green data points represent the experimental structure in panels a and b.

introduces a simple yet very powerful tool for nanoalloy design that can potentially help elucidate the energetics of alloy MNP genomes.

Methods. The DFT calculations were performed using the PBE⁶⁵ exchange—correlation functional combined with the DZVP basis set,⁶⁶ as implemented in the CP2K package.⁶⁷ PBE is ubiquitous in evaluating energetics of transition metals.^{68,69} During geometry relaxation, the energy cutoff of the basis set was 500 Ry, and there was a force cutoff of 0.0004 Ha/Bohr. A $40 \times 40 \times 40$ Å unit cell was used with all structures positioned in the center of the box. The total electronic energies of MNPs were determined from geometry relaxations performed via quasi-Newton—Raphson minimization.⁷⁰ Eq 10 was used to calculate the CE of nanoalloy A_xB_y :

$$CE_{DFT} = \frac{E_{A_x B_y} - x \times E_A - y \times E_B}{x + y}$$
(10)

=where $E_{\rm X}$ is the total electronic energy of species X.

ASSOCIATED CONTENT

S Supporting Information

The Supporting Information is available free of charge on the ACS Publications website at DOI: 10.1021/acs.nanolett.8b00670.

Detailed information on CN determination and EE derivation. Figures showing CE_{Bulk} calculations from DFT, percentages of bulk and surface atoms, chemical ordering comparisons, bulk cohesive energy, alloy MNP characteristics, parity plots, DFT-optimized geometries, and CE of randomly generated FePt alloys. (PDF)

AUTHOR INFORMATION

Corresponding Author

*E-mail: gmpourmp@pitt.edu.

ORCID ®

Giannis Mpourmpakis: 0000-0002-3063-0607

Author Contributions

Z.Y. and M.G.T contributed equally in this work. Z.Y. and M.G.T. performed the DFT calculations and python coding. A.M. performed DFT calculations on CuZr alloy MNPs. G.M. conceived the project and carried out the advising. All authors aided in the development and writing of this manuscript.

Notes

The authors declare no competing financial interest.

ACKNOWLEDGMENTS

The authors acknowledge support by the National Science Foundation (NSF) under grant no. CMMI 1634880. M.G.T. acknowledges support by the NSF Graduate Research Fellowship under grant no. 1247842. Computational support was provided by the University of Pittsburgh Center for Research Computing and the Extreme Science and Engineering Discovery Environment supported by the NSF (grant no. ACI-1548562). A.M. acknowledges support by the NSF (REU program) under grant no. 1659324.

REFERENCES

- (1) Yang, Y.; Chen, C.-C.; Scott, M. C.; Ophus, C.; Xu, R.; Pryor, A.; Wu, L.; Sun, F.; Theis, W.; Zhou, J.; Eisenbach, M.; Kent, P. R. C.; Sabirianov, R. F.; Zeng, H.; Ercius, P.; Miao, J. Deciphering chemical order/disorder and material properties at the single-atom level. *Nature* **2017**, *542* (7639), 75–79.
- (2) Talapin, D. V.; Lee, J.-S.; Kovalenko, M. V.; Shevchenko, E. V. Prospects of Colloidal Nanocrystals for Electronic and Optoelectronic Applications. *Chem. Rev.* **2010**, *110* (1), 389–458.
- (3) De, M.; Ghosh, P. S.; Rotello, V. M. Applications of Nanoparticles in Biology. *Adv. Mater.* **2008**, *20* (22), 4225–4241.
- (4) Ferrando, R.; Jellinek, J.; Johnston, R. L. Nanoalloys: From theory to applications of alloy clusters and nanoparticles. *Chem. Rev.* **2008**, *108* (3), 845–910.
- (5) Haruta, M.; Kobayashi, T.; Sano, H.; Yamada, N. Novel gold catalysts for the oxidation of carbon monoxide at a temperature far below 0°C. *Chem. Lett.* **1987**, *16*, 405–408.
- (6) Kelly, K. L.; Coronado, E.; Zhao, L. L.; Schatz, G. C. The optical properties of metal nanoparticles: The influence of size, shape, and dielectric environment. *J. Phys. Chem. B* **2003**, *107* (3), 668–677.
- (7) Yan, Y.; Warren, S. C.; Fuller, P.; Grzybowski, B. A. Chemoelectronic circuits based on metal nanoparticles. *Nat. Nanotechnol.* **2016**, *11* (7), 603–608.
- (8) Wessels, J. M.; Nothofer, H. G.; Ford, W. E.; von Wrochem, F.; Scholz, F.; Vossmeyer, T.; Schroedter, A.; Weller, H.; Yasuda, A. Optical and electrical properties of three-dimensional interlinked gold nanoparticle assemblies. *J. Am. Chem. Soc.* **2004**, *126* (10), 3349–3356.
- (9) Duan, S.; Wang, R. Bimetallic nanostructures with magnetic and noble metals and their physicochemical applications. *Prog. Nat. Sci.* **2013**, 23 (2), 113–126.
- (10) Cuenya, B. R. Synthesis and catalytic properties of metal nanoparticles: size, shape, support, composition, and oxidation state effects. *Thin Solid Films* **2010**, *518* (12), 3127–3150.
- (11) Bell, A. T. The impact of nanoscience on heterogeneous catalysis. *Science* **2003**, 299 (5613), 1688–1691.
- (12) Mpourmpakis, G.; Andriotis, A. N.; Vlachos, D. G. Identification of Descriptors for the CO Interaction with Metal Nanoparticles. *Nano Lett.* **2010**, *10* (3), 1041–1045.
- (13) Taylor, M. G.; Austin, N.; Gounaris, C. E.; Mpourmpakis, G. Catalyst Design Based on Morphology- and Environment-Dependent Adsorption on Metal Nanoparticles. *ACS Catal.* **2015**, 5 (11), 6296–6301.
- (14) Arenz, M.; Landman, U.; Heiz, U. CO combustion on supported gold clusters. *ChemPhysChem* **2006**, 7 (9), 1871–1879.

(15) Bratlie, K. M.; Lee, H.; Komvopoulos, K.; Yang, P. D.; Somorjai, G. A. Platinum nanoparticle shape effects on benzene hydrogenation selectivity. *Nano Lett.* **2007**, *7* (10), 3097–3101.

- (16) Hoare, M. R.; Pal, P. Geometry and Stability of "Spherical" f.c.c. *Nature, Phys. Sci.* **1972**, 236, 35.
- (17) Luo, L.; Duan, Z.; Li, H.; Kim, J.; Henkelman, G.; Crooks, R. M. Tunability of the Adsorbate Binding on Bimetallic Alloy Nanoparticles for the Optimization of Catalytic Hydrogenation. *J. Am. Chem. Soc.* **2017**, *139* (15), 5538–5546.
- (18) Yu, W.; Porosoff, M. D.; Chen, J. G. Review of Pt-based bimetallic catalysis: From model surfaces to supported catalysts. *Chem. Rev.* **2012**, *112* (11), 5780–5817.
- (19) Wulff, G. Zur Frage der Geschwindigkeit des Wachstums und der Auflösung der Krystallflächen. Z. Kristallogr. Cryst. Mater. 1901, 34, 449–530.
- (20) Marks, L. D.; Peng, L. Nanoparticle shape, thermodynamics and kinetics. J. Phys.: Condens. Matter 2016, 28 (5), 053001.
- (21) Ringe, E.; Van Duyne, R. P.; Marks, L. D. Kinetic and Thermodynamic Modified Wulff Constructions for Twinned Nanoparticles. *J. Phys. Chem. C* **2013**, *117*, 15859–15870.
- (22) Ringe, E.; Van Duyne, R. P.; Marks, L. D. Wulff Construction for Alloy Nanoparticles. *Nano Lett.* **2011**, *11*, 3399–3403.
- (23) Cui, M.; Lu, H.; Jiang, H.; Cao, Z.; Meng, X. Phase Diagram of Continuous Binary Nanoalloys: Size, Shape, and Segregation Effects. *Sci. Rep.* **2017**, *7*, 41990.
- (24) Guisbiers, G. Schottky Defects in Nanoparticles. *J. Phys. Chem.* C **2011**, *115* (6), 2616–2621.
- (25) Haberlen, O. D.; Chung, S. C.; Stener, M.; Rosch, N. From clusters to bulk: A relativistic density functional investigation on a series of gold clusters Au_n , $n=6,\cdots$, 147. *J. Chem. Phys.* **1997**, 106, 5189–5201.
- (26) Li, H.; Li, L.; Pedersen, A.; Gao, Y.; Khetrapal, N.; Jónsson, H.; Zeng, X. C. Magic-Number Gold Nanoclusters with Diameters from 1 to 3.5 nm: Relative Stability and Catalytic Activity for CO Oxidation. *Nano Lett.* **2015**, *15*, *682*–*688*.
- (27) Aarons, J.; Sarwar, M.; Thompsett, D.; Skylaris, C. K. Perspective: Methods for large-scale density functional calculations on metallic systems. *J. Chem. Phys.* **2016**, *145* (22).22090110.1063/1.4972007
- (28) Wang, D. L.; Xin, H. L. L.; Hovden, R.; Wang, H. S.; Yu, Y. C.; Muller, D. A.; DiSalvo, F. J.; Abruna, H. D. Structurally ordered intermetallic platinum-cobalt core-shell nanoparticles with enhanced activity and stability as oxygen reduction electrocatalysts. *Nat. Mater.* **2013**, *12* (1), 81–87.
- (29) Kozlov, S. M.; Kovacs, G.; Ferrando, R.; Neyman, K. M. How to determine accurate chemical ordering in several nanometer large bimetallic crystallites from electronic structure calculations. *Chemical Science* **2015**, *6* (7), 3868–3880.
- (30) Ducastelle, F. Tight-Binding potentials for transition metals and alloys. *Computer Simulation in Materials Science* **1991**, 48 (1), 233–253.
- (31) Ackland, G. J.; Finnis, M. W.; Vitek, V. Validity of the second moment tight-binding model. *J. Phys. F: Met. Phys.* **1988**, *18* (8), L153.
- (32) Rosato, V.; Guillope, M.; Legrand, B. Thermodynamical and structural properties of f.c.c. transition metals using a simple tight-binding model. *Philos. Mag. A* **1989**, *59* (2), 321–336.
- (33) Papanicolaou, N. I.; Kallinteris, G. C.; Evangelakis, G. A.; Papaconstantopoulos, D. A.; Mehl, M. J. Second-moment interatomic potential for Cu-Au alloys based on total-energy calculations and its application to molecular-dynamics simulations. *J. Phys.: Condens. Matter* 1998, 10 (48), 10979.
- (34) Daw, M. S.; Baskes, M. I. Embedded-atom method: Derivation and application to impurities, surfaces, and other defects in metals. *Phys. Rev. B: Condens. Matter Mater. Phys.* **1984**, 29 (12), 6443–6453.
- (35) Daw, M. S.; Foiles, S. M.; Baskes, M. I. The embedded-atom method a review of theory and applications. *Mater. Sci. Rep.* **1993**, *9* (7–8), 251–310.

(36) Jacobsen, K. W.; Stoltze, P.; Norskov, J. K. A semi-empirical effective medium theory for metals and alloys. *Surf. Sci.* **1996**, *366* (2), 394–402.

- (37) Finnis, M. W.; Sinclair, J. E. A simple empirical n-body potential for transition-metals. *Philos. Mag. A* **1984**, *50* (1), 45–55.
- (38) Sutton, A.; Chen, J. Long-range Finnis-Sinclair potentials. *Philos. Mag. Lett.* **1990**, *61*, 139–146.
- (39) Shi, H.; Koskinen, P.; Ramasubramaniam, A. Self-Consistent Charge Density-Functional Tight-Binding Parametrization for Pt—Ru Alloys. J. Phys. Chem. A 2017, 121 (12), 2497—2502.
- (40) Onat, B.; Durukanoğlu, S. An optimized interatomic potential for Cu–Ni alloys with the embedded-atom method. *J. Phys.: Condens. Matter* **2014**, *26* (3), 035404–035404.
- (41) Kovács, G.; Kozlov, S. M.; Neyman, K. M. Versatile Optimization of Chemical Ordering in Bimetallic Nanoparticles. *J. Phys. Chem. C* **2017**.1211080310.1021/acs.jpcc.6b11923
- (42) Peng, L.; Ringe, E.; Van Duyne, R. P.; Marks, L. D. Segregation in bimetallic nanoparticles. *Phys. Chem. Chem. Phys.* **2015**, *17*, 27940–27951.
- (43) Methfessel, M.; Hennig, D.; Scheffler, M. Calculated surface energies of the 4 d transition metals: A study of bond-cutting models. *Appl. Phys. A: Solids Surf.* **1992**, *55*, 442–448.
- (44) Tomanek, D.; Mukherjee, S.; Bennemann, K. H. Simple theory for the electronic and atomic structure of small clusters. *Phys. Rev. B: Condens. Matter Mater. Phys.* **1983**, 28, 665–673.
- (45) Tomanek, D.; Aligia, A. A.; Balseiro, C. A. Calculation of elastic strain and electronic effects on surface segregation. *Phys. Rev. B: Condens. Matter Mater. Phys.* **1985**, 32 (8), 5051–5056.
- (46) Zhong, W.; Li, Y. S.; Tomanek, D. Effect of adsorbates on surface phonon modes H on Pd(001) and Pd(110). *Phys. Rev. B: Condens. Matter Mater. Phys.* **1991**, 44 (23), 13053–13062.
- (47) Taylor, M. G.; Mpourmpakis, G. Thermodynamic Stability of Ligand-Protected Metal Nanoclusters. *Nat. Commun.* **2017**, *8*, 15988. (48) Kittel, C. Introduction to Solid State Physics. *Am. J. Phys.* **2004**, 35, 547.
- (49) Gražulis, S.; Chateigner, D.; Downs, R. T.; Yokochi, A. F. T.; Quirós, M.; Lutterotti, L.; Manakova, E.; Butkus, J.; Moeck, P.; Le Bail, A. Crystallography Open Database an open-access collection of crystal structures. *J. Appl. Crystallogr.* **2009**, *42* (4), 726—729.
- (50) Larsen, A. H.; Mortensen, J. J.; Blomqvist, J.; Castelli, I. E.; Christensen, R.; Dulak, M.; Friis, J.; Groves, M. N.; Hammer, B.; Hargus, C.; et al. The atomic simulation environment—a Python library for working with atoms. *J. Phys.: Condens. Matter* **2017**, 29 (27), 273002.
- (51) Wang, H.; Zhou, S.; Gilroy, K. D.; Cai, Z.; Xia, Y. Icosahedral nanocrystals of noble metals: Synthesis and applications. *Nano Today* **2017**, *15*, 121–144.
- (52) Austin, N.; Ye, J.; Mpourmpakis, G. CO₂ activation on Cu-based Zr-decorated nanoparticles. *Catal. Sci. Technol.* **2017**, *7* (11), 2245–2251.
- (53) Sneed, B. T.; Young, A. P.; Tsung, C.-K. Building up strain in colloidal metal nanoparticle catalysts. *Nanoscale* **2015**, 7 (29), 12248–12265.
- (54) Eberhart, J. G.; Horner, S. Bond-Energy and Surface-Energy Calculations in Metals. *J. Chem. Educ.* **2010**, 87 (6), 608–612.
- (55) Linic, S.; Christopher, P.; Ingram, D. B. Plasmonic-metal nanostructures for efficient conversion of solar to chemical energy. *Nat. Mater.* **2011**, *10*, 911–921.
- (56) Van Aert, S.; Batenburg, K. J.; Rossell, M. D.; Erni, R.; Van Tendeloo, G. Three-dimensional atomic imaging of crystalline nanoparticles. *Nature* **2011**, 470 (7334), 374–377.
- (57) Chen, C.-C.; Zhu, C.; White, E. R.; Chiu, C.-Y.; Scott, M. C.; Regan, B. C.; Marks, L. D.; Huang, Y.; Miao, J. Three-dimensional imaging of dislocations in a nanoparticle at atomic resolution. *Nature* **2013**, 496 (7443), 74–77.
- (58) Bals, S.; Casavola, M.; Van Huis, M. A.; Van Aert, S.; Batenburg, K. J.; Van Tendeloo, G.; Vanmaekelbergh, D. Three-dimensional atomic imaging of colloidal core-shell nanocrystals. *Nano Lett.* **2011**, *11* (8), 3420–3424.

- (59) Goris, B.; De Backer, A.; Van Aert, S.; Gómez-Graña, S.; Liz-Marzán, L. M.; Van Tendeloo, G.; Bals, S. Three-dimensional elemental mapping at the atomic scale in bimetallic nanocrystals. *Nano Lett.* **2013**, *13* (9), 4236–4241.
- (60) Morse, M. D. Clusters of transition-metal atoms. *Chem. Rev.* **1986**, *86* (6), 1049–1109.
- (61) Miedema, A. R. Model predictions of the dissociation energies of homonuclear and heteronuclear diatomic molecules of two transition metals. *Faraday Symp. Chem. Soc.* **1980**, *14* (0), 136–148.
- (62) McDavid, J. M.; Fain, S. C. Segregation at Cu-Au alloy surfaces. Surf. Sci. 1975, 52 (1), 161–173.
- (63) Guedes-Sobrinho, D.; Nomiyama, R. K.; Chaves, A. S.; Piotrowski, M. J.; Da Silva, J. L. F. Structure, Electronic, and Magnetic Properties of Binary Pt_nTM_{55-n} (TM = Fe, Co, Ni, Cu, Zn) Nanoclusters: A Density Functional Theory Investigation. *J. Phys. Chem. C* **2015**, *119* (27), 15669–15679.
- (64) Piotrowski, M. J.; Piquini, P.; Da Silva, J. L. F. Platinum-Based Nanoalloys Pt_nTM_{5S-n} (TM = Co, Rh, Au): A Density Functional Theory Investigation. *J. Phys. Chem. C* **2012**, *116* (34), 18432–18439.
- (65) Perdew, J. P.; Burke, K.; Ernzerhof, M. Generalized gradient approximation made simple. *Phys. Rev. Lett.* **1996**, 77 (18), 3865–3868
- (66) VandeVondele, J.; Hutter, J. Gaussian basis sets for accurate calculations on molecular systems in gas and condensed phases. *J. Chem. Phys.* **2007**, *127* (11).11410510.1063/1.2770708
- (67) Hutter, J.; Iannuzzi, M.; Schiffmann, F.; VandeVondele, J. CP2K: atomistic simulations of condensed matter systems. *Wiley Interdiscip. Rev.-Comput. Mol. Sci.* **2014**, *4* (1), 15–25.
- (68) Yoon, Y.; Rousseau, R.; Weber, R. S.; Mei, D. H.; Lercher, J. A. First-Principles Study of Phenol Hydrogenation on Pt and Ni Catalysts in Aqueous Phase. *J. Am. Chem. Soc.* **2014**, *136* (29), 10287–10298.
- (69) Wang, Y. G.; Mei, D. H.; Glezakou, V. A.; Li, J.; Rousseau, R. Dynamic formation of single-atom catalytic active sites on ceria-supported gold nanoparticles. *Nat. Commun.* **2015**, *6*, 8.
- (70) Byrd, R.; Lu, P.; Nocedal, J.; Zhu, C. A Limited Memory Algorithm for Bound Constrained Optimization. *SIAM Journal on Scientific Computing* **1995**, *16* (5), 1190–1208.